Research Paper

The impact of rheology model choices on tidal heating studies

Carver J. Bierson

School of Earth and Space Exploration, Arizona State University, Tempe, AZ, 85281, USA

ARTICLE INFO

ABSTRACT

Every study modeling tidal heating must adopt some rheology model. Rheology models describe the relationship between the imposed stress, and the resulting deformation (strain). There are a wealth of rheology models that have been developed to describe experimental and seismic data. In this work I collate a wide range of experimental data and compare it to rheology models that are commonly used in tidal heating studies. I use this data set to constrain values of the dimensionless Andrade parameter ζ. I find that the resulting ζ values vary by orders of magnitude, far more than is typically explored in tidal heating studies. For the case of Europa's mantle, this could imply much more tidal heating in the silicate mantle than has been previously suggested.

1. Introduction

Tidal heating is the dominant heat source for many worlds in the outer solar system. Tidal heating powers Io's volcanism, Europa's subsurface ocean, and Enceladus's geysers. Because of the importance of this process, there is broad literature modeling tidal heating with a variety of methods. In this work I perform a detailed estimation of the existing rheology models and their ability to extrapolate from the lab to planetary conditions.

1.1. Background on Tidal heating

Tidal heating involves many scales; from the orbit, to the structure of the body, to the grain-scale. At the level of the orbit, tidal heating takes energy from the orbit and, via friction, dissipates it within the body (Murray and Dermott, 1999). For eccentricity tides, this gradually decreases the eccentricity, circularizing the orbit over time. Unless there is some other process, such as gravitational interactions with other bodies, this will drive the eccentricity to zero (Yoder, 1979; Ojakangas and Stevenson, 1986).

The amount of tidal dissipation, $\dot{E}$, caused by eccentricity tides for a synchronously rotating, low eccentricity satellite can be described by

$$\dot{E} = -\frac{21}{2} Im(k_2^*) \frac{\omega^5 R^5}{G_g} e^2. \tag{1}$$

Here ω is the orbital angular frequency (mean motion), R is the radius of the body experiencing the heating, e is the orbital eccentricity, and G_g is the universal gravitational constant. All of the information about the rheology and structure of the world is in the term $Im(k_2^*)$. All symbols used in this work, and their nominal values where appropriate, are listed in Table 1.

The complex tidal potential Love number is given by k_2^*. The real part describes the total strength of a planetary body. For a fluid world (no strength) $Re(k_2^*) = 3/2$ and for a body of infinite strength $Re(k_2^*)$ goes to zero. The imaginary part is related to the phase lag between the tide raising potential and the tidal potential response. See Section 2 for more detail on the relationship to this phase lag.

For a uniform body, the complex potential Love number is given by

$$k_2^* = \frac{3}{2} \frac{1}{1 + \frac{19}{2} \frac{G^*}{\rho g R}} \tag{2}$$

Here ρ is the body density, g is the gravitational acceleration, and G^* is the complex shear modulus (described in detail in Section 1.2). It is important to emphasize here that k_2^* is a strong function of frequency, inherited from G^*. No tidally heated world is a uniform body, however Eq. (2) serves as a useful tool in exploring how changes in rheology impact tidal heating in a general sense. The limitations of this approach will be discussed in Section 6.

It is common in the literature to substitute

$$-Im(k_2^*) = |k_2^*|/Q_t. \tag{3}$$

The term Q_t is the tidal "quality factor" and generally describes the energy dissipated per cycle (ΔE) relative to the energy stored in the system (E). This is given by

$$Q^{-1} = \frac{\Delta E}{2\pi E} \tag{4}$$

Eq. (3) is equivalent to the statement $Q_t^{-1} = \sin(\phi)$ where ϕ is the tidal phase lag. I discuss this in detail in Section 2.

E-mail address: cbierson@asu.edu.

Table 1
All variables used throughout this work and there nominal values where appropriate.

Name	Symbol	Nominal value (range)	Units	Source
Frequency	f	3×10^{-6}	s^{-1}	
Maxwell frequency	f_M		s^{-1}	
Angular frequency	ω		s^{-1}	
Normalized angular frequency	ω_N			
Pseudo-period angular frequency	ω_X		s^{-1}	
Orbital eccentricity	e			
Viscosity	η	10^{20}	Pa s	
Reference viscosity	η_R		Pa s	
Universal gravitational constant	G_g	6.674×10^{-11}	$m^3 \ kg^{-1} \ s^{-2}$	
Shear modulus	G		Pa	
Unrelaxed shear modulus	G_0	50×10^9	Pa	
Reference unrelaxed shear modulus	G_{0R}		Pa	
Complex compliance	J^*		Pa^{-1}	
Complex gravitational potential Love number	k_2^*			
Temperature	T		K	
Reference Temperature	T_R	1173.15	K	
Quality factor	Q			
Energy	E		J	
Grain size	d		m	
grain size exponent	m			
Viscosity activation energy	E_η	300×10^3	$J \ mol^{-1}$	
Universal gas constant	R	8.314	$J \ mol^{-1} \ K^{-1}$	
Rheological dissipation exponent	n	0.33		
Bulk density	ρ	3010	$kg \ m^{-3}$	
Gravitational acceleration	g	1.3	$m \ s^{-2}$	
Radius	R	1821×10^3	m	
Bulk density	ρ	3010	$kg \ m^{-3}$	
Gravitational stress	σ_g		Pa	Eq. (18)
Uncertainty	$\sigma_{variable}$			
Andrade Parameter	β	10^{-12}	$Pa \ s^{-n}$	
Normalized Andrade parameter	β^*	0.02	s^{-n}	
Normalized Andrade timescale	ζ	1.0		Castillo-Rogez et al. (2011)
Burgers	Δ	1.0		
Maxwell time	τ_M		s	
Burgers time upper limit	τ_H	τ_M	s	Faul and Jackson (2015)
Burgers time lower limit	τ_L	10^{-2}	s	
Tidal phase angle	ϕ			
Seismic phase angle	ϵ			

1.2. Existing rheology models and their applications

Rheology models are the bridge between the material properties of a planetary body (viscosity, density, elastic modulus) and the tidal Love number needed to estimate tidal dissipation. Rheology models are typically described in terms of their complex compliance, J^*. The complex compliance can be related to the complex elastic modulus by

$$G^* = J^{*-1} \tag{5}$$

When describing the complex compliance I use the following convention

$$J^* = J_1 - iJ_2. \tag{6}$$

This can be related to the elastic modulus (generally the shear modulus for tidal heating studies) and the seismic quality factor via

$$G = |G^*| = \left[\sqrt{J_1^2 + J_2^2} \right]^{-1} \tag{7}$$

$$Q_s^{-1} = J_2/J_1. \tag{8}$$

This definition of Q_s assumes the energy term in Eq. (4) is the average energy in the system (see Section 2).

The complex compliance describes the strain response of a material to stress. In the frequency domain, rheological models generally take the form

$$J^* = \underbrace{\frac{1}{G_0}}_{\text{Elastic}} - i \underbrace{\frac{1}{\omega\eta}}_{\text{Viscous}} + \text{Anelastic Term}. \tag{9}$$

Here G_0 is the unrelaxed (infinite frequency) shear modulus, η is the viscosity, and ω is the forcing angular frequency. The angular and linear frequency f, are related by

$$\omega = 2\pi f. \tag{10}$$

In Eq. (9), the elastic term describes deformation that is instantly recovered. The viscous term describes deformation that is not recovered when the stress is removed. The anelastic term describes deformation that is recoverable, but not instantly. These types of deformation are reviewed in Jackson et al. (2014). This equation shows that at very short periods (high frequency) materials generally behaves elastically, and at very long periods, viscously. The anelastic term has the most variation between different rheological models.

The simplest rheological model is the Maxwell model, which includes no anelastic term. The Maxwell model has been, and continues to be, extensively used in the tidal heating literature (Moore and Schubert, 2000; Sotin et al., 2002; Hussmann et al., 2002; Hussmann and Spohn, 2004; Nimmo, 2004; Tobie et al., 2005; Moore, 2006; Roberts and Nimmo, 2008; Sotin et al., 2009; Mitri, 2023). However the Maxwell rheology model does not match experimental dissipation studies because it lacks any anelastic response.

The Maxwell model does provide a clear characteristic timescale, known as the Maxwell time

$$\tau_M = \frac{\eta}{G_0}. \tag{11}$$

This is the timescale at which elastic and viscous deformation are equivalent in magnitude. It has been suggested that this timescale allows for a scaling between otherwise very different materials (Morris

and Jackson, 2009; McCarthy et al., 2011), a topic that will be explored in detail in Section 5.

The most commonly used alternative rheological model in tidal heating studies has become the Andrade model (Andrade, 1910). There are least two different versions of the Andrade model that have been used in tidal heating studies, and a third variation present in the experimental literature. Table 2 describes each of these models and the naming convention that will be used in this paper. Each of these variations has a slightly different dependence on viscosity, the importance of which will be shown in Sections 3 and 5.

All version of the Andrade rheology have a exponent on the time (or frequency) dependence of deformation. This exponent, here called n, was initially estimated to be 1/3 by Andrade (1910) and this will be the default value used here (Table 1). More recent studies have found values of n generally fall between 0.2–0.4 (Tan et al., 2001; Jackson et al., 2002, 2004; Jackson and Faul, 2010).

The first version of the Andrade model is the β model. This model has been applied to the tidal heating of Io (Bierson and Nimmo, 2016; Abrahams, 2022), lunar tides (Xiao et al., 2022), the despinning of Eris (Nimmo and Brown, 2023) and tidal dissipation in multi-phase systems (Kamata, 2023). One limitation of this rheology is that the controlling parameter, β, is a function of the material composition, grain-size, and its temperature (Jackson et al., 2002). Experimentally determined values of β range between $10^{-12} - 3 \times 10^{-11}$ Pa s^{-n} as shown in Fig. 4 (Tan et al., 2001; Jackson et al., 2002, 2004). In this work I use a nominal value of $\beta = 10^{-12}$ Pa s^{-n}.

In an effort to make this model scale more directly with viscosity, the ζ model was developed (Castillo-Rogez et al., 2011; Efroimsky, 2012b). This has since become the most widely used, non-Maxwell, model in tidal heating studies (Shoji et al., 2013; Renaud and Henning, 2018; Saxena et al., 2018; Gevorgyan et al., 2020; Běhounková et al., 2021; Rhoden and Walker, 2022; Xiao et al., 2022). For this model it is generally assumed that $\zeta = 1.0$ following arguments from Castillo-Rogez et al. (2011) and Efroimsky (2012b). This assumption will be directly evaluated in Section 4.

Separately, the experimental community modified the Andrade model to the β^* version (Jackson and Faul, 2010). This model uses a pseudoperiod scaling on the forcing timescale itself. Jackson et al. (2004) argues that this style of pseudoperiod scaling allows for a better transition from anelastic to viscous behavior. This β^* rheology has been utilized by the Earth seismic and tidal modeling community (Khan et al., 2018; Bagheri et al., 2019). Jackson and Faul (2010) estimate a best fit value of $\beta^* = 0.02$ which will be used throughout this work.

Some tidal heating studies also have used the Extended Burgers model, usually alongside Andrade (Shoji et al., 2013; Renaud and Henning, 2018). The Extended Burgers model, as given by Jackson and Faul (2010) is described by

$$J_1 = \frac{1}{G_0(T)} \left[1 + \Delta \int_{\tau_L}^{\tau_H} \frac{D(\tau)}{1 + \omega^2 \tau^2} d\tau \right] \quad (12)$$

$$J_2 = \frac{1}{G_0(T)} \left[\frac{1}{\omega \tau_M} + \omega \Delta \int_{\tau_L}^{\tau_H} \frac{\tau D(\tau)}{1 + \omega^2 \tau^2} d\tau \right] \quad (13)$$

$$D_B(\tau) = \frac{n \tau^{n-1}}{\tau_H^n - \tau_L^n} \quad (14)$$

Here Δ determines the magnitude of the anelastic response and τ_L and τ_H determine the lower and upper timescale bounds over which the anelastic response is present. Across a range of experimental studies Δ has been estimated to be between $10^{-1} - 10$ with values centered around 1.0 (Tan et al., 2001; Jackson et al., 2002; Jackson and Faul, 2010). In this work I use a nominal value of $\Delta = 1.0$ (see Appendix B for more detail). I assume $\tau_L = 10^{-2}$ following Jackson and Faul (2010). Faul and Jackson (2015) argue that $\tau_H = \tau_M$ as the anelastic behavior transitions to viscous, an assumption I will apply in this study.

Jackson and Faul (2010) and Faul and Jackson (2015) also add the option of including an additional dissipation peak in the Burgers model. This second peak generally captures additional dissipation from

Table 2

Rheology models, and the name for each used in this text. For the normalized models, $\omega_N \equiv \omega \left(\frac{\eta}{G_0} \right)$.

Model name	Complex compliance
Maxwell	$J^* = \frac{1}{G_0(T)} - i \frac{1}{\omega \eta(d,T)}$
Andrade β	$J^* = \frac{1}{G_0(T)} - i \frac{1}{\omega \eta(d,T)} + \beta(d,T)(i\omega)^{-n} \Gamma(n+1)$
Andrade β^*	$J^* = \frac{1}{G_0(T)} \left[1 - i \frac{1}{\omega_X(d,T)\tau_M} + \beta^* \left(i\omega_X(d,T) \right)^{-n} \Gamma(n+1) \right]$
	$\omega_X = 2\pi \left[P \left(\frac{d}{d_0} \right)^{-m} \exp \left(\frac{-E_g}{R} \left(\frac{1}{T} - \frac{1}{T_R} \right) \right) \right]^{-1}$
Andrade ζ	$J^* = \frac{1}{G_0(T)} - i \frac{1}{\omega \eta(d,T)} + \frac{1}{G_0(T)} \left(\zeta \frac{\eta(d,T)}{G_0(T)} i\omega \right)^{-n} \Gamma(n+1)$
Extended Burgers	See text (Eqs. (12) and (13))
	Normalized models
Maxwell Norm	$J^* = \frac{1}{G_0(T)} \left[1 - i \frac{1}{\omega_N} \right]$
Andrade β Norm	$J^* = \frac{1}{G_0(T)} - i \frac{1}{\omega_N G_0(T)} + \beta(d,T) \left(\frac{\eta}{G_0} i\omega_N \right)^{-n} \Gamma(n+1)$
Andrade ζ Norm	$J^* = \frac{1}{G_0(T)} \left[1 - i \frac{1}{\omega_N} + (i\zeta\omega_N)^{-n} \Gamma(n+1) \right]$

other dissipation mechanisms. In the case of Jackson et al. (2004) this additional dissipation is from partial melt in the samples. Sundberg and Cooper (2010) also describe an additional dissipation peak caused by elastically accommodated grain boundary sliding. Because there is not a generally agreed upon set of parameters for this second peak it will not be used in this work.

Fundamentally, the rheological models presented in this work are all aiming to describe the behavior of polycrystalline materials under a particular deformation regime. In the regime relevant to this work, deformation is primarily accommodated by sliding at grain boundaries. Defects in the material can be of particular importance in allowing deformation (Raj and Ashby, 1971; Findley et al., 1976; Tan et al., 2001; McCarthy et al., 2011). As such, the abundance and style of defects impacts the anelastic parameters discussed above. For more on the connection between the generalized mathematical models presented here, and the grain scale root causes I suggest the summaries in Faul and Jackson (2015), Renaud and Henning (2018), and the references therein. In this work I focus on the constraints on these anelastic parameters, but not their deeper connection to grain scale processes.

1.3. Experiments on seismic attenuation

The most direct way to test any rheology model is through the laboratory experiments. The experimental rheology studies presented here are generally motivated by trying to understand variations in seismic wave velocities in Earth's upper mantle. These experiments must replicate the deformation mechanisms present in the mantle (primarily grain boundary sliding), at far lower pressures, while avoiding thermal microcracking, and under conditions for which seismic attenuation will be large enough to be accurately measured (Jackson et al., 2002; Jackson and Faul, 2010). These constraints push studies to use grain sizes in the lab (1–100 μm) that are typically orders of magnitude smaller than are present in the mantle (~1000 μm) (Karato, 1984; Faul and Jackson, 2005; Behn et al., 2009). Correspondingly, this leads to viscosity values between $10^{11} - 10^{16}$ Pa s (Gribb and Cooper, 1998; Tan et al., 2001; Jackson et al., 2002, 2004; Jackson and Faul, 2010; Sundberg and Cooper, 2010) while the viscosity of Earth's upper mantle is typically thought to be $\sim 10^{21}$ Pa s (Cathles, 1975; Sabadini and Peltier, 1981; Peltier, 1996; Lau and Holtzman, 2019). It is then the role of rheology models to extrapolate from the laboratory conditions to the mantle (or planetary tides).

Experimental studies have used a variety of materials as well. The majority of studies use poly-crystalline olivine (Gribb and Cooper, 1998; Tan et al., 2001; Jackson et al., 2002, 2004; Jackson and Faul, 2010; Sundberg and Cooper, 2010). Some recent studies have measured attenuation in polycrystalline MgO (Barnhoorn et al., 2016) and olivine-pyroxene mixtures (Qu et al., 2021). Other works have used
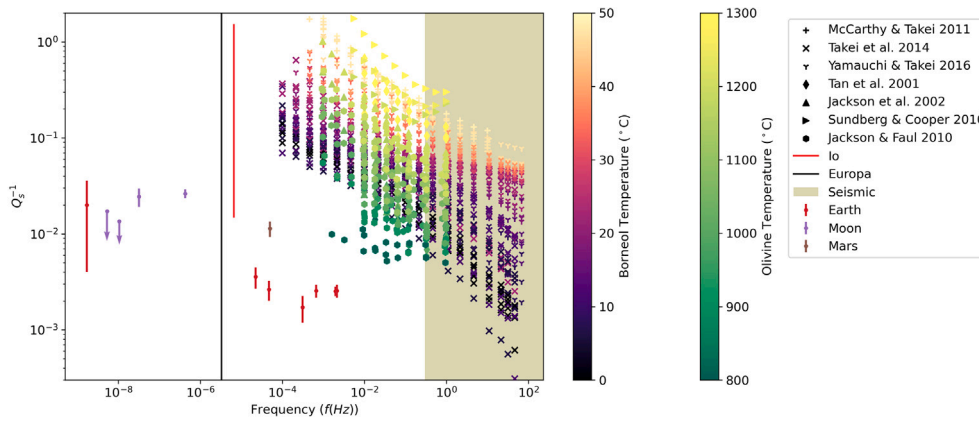
Fig. 1. Planetary tides are far lower frequency than the existing experimental data. These same datasets are later plotted against the normalized frequency in Fig. 7. That figure shows that lower frequency data is not necessarily the solution to better understanding rheology in the tidal regime.

polycrystalline organic borneol (McCarthy et al., 2011; McCarthy and Takei, 2011; Takei et al., 2014; Yamauchi and Takei, 2016). Borneol has a significantly lower melting temperature than olivine (205 °C) allowing for lower temperature experiments to incorporate partial melting. McCarthy and Cooper (2016) performs similar experiments on water ice.

McCarthy et al. (2011) argues that the mechanism of dissipation is the same in all poly-crystalline materials, and thus all these materials can inform the rheological models. There is a caveat that this dissipation scaling only applies when grain boundary sliding is the dominant deformation mechanism (McCarthy et al., 2011). Grain boundary sliding is the expected dominant deformation mechanism in all of the contexts used in this work (Castillo-Rogez et al., 2011). This scaling of dissipation will be discussed again in Section 5.

As shown in Fig. 1, experiments on olivine have been performed at a range of frequencies between 10^{-4} and 10^0 Hz. This is lower than seismic waves which have most of their power in frequencies > 1 Hz. At the same time it is much higher than tidal frequencies which range from 5×10^{-5} Hz (Mars-Phobos) to 4×10^{-7} Hz (Earth–Moon). From this it could be argued that longer period data is needed to better understand tidal heating systems. However because of other differences between lab samples and planetary mantles, I will argue against this in Section 6. The connection, and differences, between seismic and planetary Q^{-1} values will be discussed in detail in Section 2.

1.4. Estimates of planetary Q_t

Because tidal forces modify the orbits of moons, close measurements of orbital variations can be used to determine $Im(k_2^*)$. However, due to the high level of precision required, this has only been performed for four terrestrial worlds. When $Re(k_2^*)$ can be independently measured, Eq. (3) allows for an estimate of the planetary Q_t at a given frequency. Here I review the available observations and their limitations (summarized in Table 3).

The most precise observations are available for the Earth and Moon. For the Earth, a range of Q_s estimates at normal mode frequencies have been determined from seismic data (Sailor and Dziewonski, 1978; Lau and Holtzman, 2019). At tidal frequencies to estimate Q_t the solid body response of the Earth must be decoupled form the response of the ocean and atmosphere. This has been done for two separate periods of 12.5 h and 18.6 years (Ray et al., 2001; Benjamin et al., 2006).

For the Moon, high precision orbital tracking has been enabled by the Apollo retro-reflectors and lunar laser ranging. This dataset has been analyzed to determine the lunar $Im(k_2^*)$ at four periods (Williams and Boggs, 2015). From the GRAIL lunar gravity measurements the lunar $Re(k_2^*)$ is also known for the lunar orbital frequency (Williams et al., 2014). If one assumes that the change in $Re(k_2^*)$ is small between

these frequencies, Q_t can also be estimated (Williams and Boggs, 2015; Xiao et al., 2022; Walterová et al., 2023a).

At Mars, precise measurements of the orbit of the inner satellite Phobos allow for the determination of $Im(k_2^*)$ of Mars at the synodic period of Phobos (Bills et al., 2005). Independent estimates for $Re(k_2^*)$ at the solar tide frequency have been determined by Yoder et al. (2003). Because Phobos is so close to Mars, higher order terms (k_3, k_4) are required to model the orbital changes. In this work I will use the Q_t estimate from Nimmo and Faul (2013), which is a slight adjustment on the value determined by Bills et al. (2005).

Jupiter's moon Io is the most volcanically active world in the solar system. This volcanism is driven by tidal heating. Because of this, estimates of the total heat flow can be used to estimate $Im(k_2^*)$ using Eq. (1), assuming they are in steady state (Moore et al., 2007). Astrometric tracking of Io's orbit has also been used to determine $Im(k_2^*)$ and these estimates agree within their error (Lainey et al., 2009). However, Io's $Re(k_2^*)$ is not known at tidal frequencies. The fluid k_2 (i.e. infinite period) has been estimated from the Galileo spacecraft tracking to be 1.2924 ± 0.0027 (Anderson et al., 2001). However, there is no direct way to estimate $Re(k_2^*)$ at tidal frequencies from this value. Depending on Io's internal structure, Bierson and Nimmo (2016) predict the tidal $Re(k_2^*)$ could be between $0.09 - 0.5$.

2. Differences between the seismic and planetary Q

In both laboratory seismic attenuation studies and planetary tidal dissipation work the "quality factor", Q is given by Eq. (4). However the energy term in this equation, E, is interpreted in different ways in the planetary and seismic communities. In this Section 1 describe the relationship between the seismic and tidal Q.

In the planetary literature, E is treated to be the maximum energy stored in the system over one cycle (Knopoff and MacDonald, 1958; Goldreich and Gold, 1963). This results in the tidal Q_t

$$Q_t^{-1} = -Im(k_2^*)/|k_2^*| = \sin(\phi) \tag{15}$$

where ϕ is the phase lag between the tidal potential bulge and the tide raising primary (Efroimsky, 2012a).

In the experimental rheology community, E is treated to be the average energy in the system over one cycle. This choice is often cited to O'Connell and Budiansky (1978) who argued that the maximum energy cannot be directly related to the rheology of the material. Using this average energy definition, the seismic Q_s is defined as

$$Q_s^{-1} = -Im(J^*)/Re(J^*) = \tan(\epsilon) \tag{16}$$

where ϵ is the phase lag between the forcing stress and resulting strain O'Connell and Budiansky (1978).

Table 3
Measured k_2 and Q values for planetary bodies and the associated periods.

World	Period	$|k_2^*|$	Q	$-Im(k_2^*) = |k_2^*|/Q_t$	Source(s)
Earth					
	470 s		390 ± 60[c]		Lau and Faul (2019), https://igppweb.ucsd.edu/~gabi/rem.html
	510 s		395 ± 45[c]		Lau and Faul (2019), https://igppweb.ucsd.edu/~gabi/rem.html
	1500 s		390 ± 60[c]		Lau and Faul (2019), https://igppweb.ucsd.edu/~gabi/rem.html
	2100 s		380 ± 90[c]		Lau and Faul (2019), https://igppweb.ucsd.edu/~gabi/rem.html
	3200 s		580 ± 180[c]		Sailor and Dziewonski (1978), Lau and Faul (2019)
	12.5 h		280 ± 70		Ray et al. (2001)
	18.6 years	0.340 ± 0.02		0.013 ± 0.007	Benjamin et al. (2006)
Moon					
	seismic	0.0232			Weber et al. (2011)
	27.2 days	0.02416 ± 0.00022			Williams et al. (2014)
	27.2 days		38 ± 4[b]	$(6.4 \pm 1.5) \times 10^{-4}$	Williams and Boggs (2015)
	1 year		41 ± 9[b]	$(6.2 \pm 1.4) \times 10^{-4}$	Williams and Boggs (2015)
	3 years		≥ 74[b]	$\leq 3.5 \times 10^{-4}$	Williams and Boggs (2015)
	6 years		≥ 58[b]	$\leq 4.5 \times 10^{-4}$	Williams and Boggs (2015)
Mars					
	24.66 h	0.149 ± 0.017			Yoder et al. (2003)
	5.55 h	0.148 ± 0.017[a]	88 ± 16		Bills et al. (2005), Nimmo and Faul (2013)
Io	1.77 days			0.015 ± 0.003	Lainey et al. (2009)

[a] Determined using a model to adjust the value from Yoder et al. (2003) to Phobos' period.
[b] Values derived assuming constant $Re(k_2^*)$.
[c] These values are for Q_s and are derived from seismic modes.

For deriving the relationship between Q_t and Q_s, it is useful to define the magnitude of the compliance

$$J = |J^*| \tag{17}$$

in addition to

$$\sigma_g = \frac{2}{19}\rho g R \tag{18}$$

This term, σ_g, I will refer to as the gravitational stress. This is an imperfect name as it is not the average or maximum gravitational stress of the body. However, when compared with the strength of the body, this will determine if the world is in a strength or gravity dominated regime.

Following Efroimsky (2012b) and Renaud and Henning (2018), I can write the real and imaginary parts of Eq. (2) (for a uniform body) as

$$Re(k_2^*) = \frac{3}{2} \frac{J_1/\sigma_g + J^2}{J_2^2/(\sigma_g^2 J^2) + \left[J_1/\sigma_g + J^2\right]^2} \tag{19}$$

$$Im(k_2^*) = -\frac{3}{2} \frac{J_2/\sigma_g}{J_2^2/(\sigma_g^2 J^2) + \left[J_1/\sigma_g + J^2\right]^2} \tag{20}$$

I can write the tidal Q_t (Eq. (15)) as

$$Q_t^{-1} = \frac{-Im(k_2^*)}{\sqrt{Re(k_2^*)^2 + Im(k_2^*)^2}} \tag{21}$$

I will start by approximating $Re(k_2^*)^2 \gg Im(k_2^*)^2$. This is equivalent to the small angle approximation, $\tan(\phi) \approx \sin(\phi)$. For the available observations of Q_t, this approximation is very strong (Table 3). I then substitute in Eqs. (19) and (20) into Eq. (21)

$$Q_t \approx -\frac{Re(k_2^*)}{Im(k_2^*)} \tag{22}$$

$$= \frac{J_1 + J^2 \sigma_g}{J_2} \tag{23}$$

$$= \frac{J_1}{J_2} + \frac{J^2 \sigma_g}{J_2} \tag{24}$$

$$Q_t = Q_s + \frac{J^2 \sigma_g}{J_2} \tag{25}$$

$$\implies Q_t/Q_s = \frac{1}{1 + \frac{J^2 \sigma_g}{J_1}} \tag{26}$$

Table 4
Values of the gravitational stress (Eq. (18)) for the relevant worlds.

	σ_g (GPa)
Earth	36
Mars	5.2
Moon	0.98
Io	1.2
Europa	0.64

To this point, this derivation is independent of any particular rheology model. It is illustrative to insert a Maxwell rheology into Eq. (26). Here I will use the normalized form shown in Table 2 that uses the angular frequency normalized by the Maxwell time ($\omega_N = \omega \tau_M$). This results in

$$Q_t/Q_s = \frac{G_0/\sigma_g}{1 + G_0/\sigma_g + 1/\omega_N^2}. \tag{27}$$

For planetary tides it is often the case that the forcing period is much faster than the Maxwell time and therefore $\omega_N \gg 1$, in which case the above expression simplifies to

$$Q_t/Q_s \approx \frac{G_0/\sigma_g}{1 + G_0/\sigma_g} \tag{28}$$

This form only depends on G_0/σ_g, a term which past work have referred to as the normalized strength (Efroimsky, 2012a; Renaud and Henning, 2018).

A direct comparison of Q_t and Q_s is shown for $\sigma_g = 0.64$ (Europa) with a Maxwell rheology in Fig. 2. In this example, when the forcing frequency is equal to or larger than the Maxwell frequency, $Q_t/Q_s \approx 0.8$. It is only for cases where $\omega_N \ll 1$ (the gravity dominated regime) that these quantities strongly diverge. The peak in Q_t is a frequency ~20 times lower than the Maxwell frequency as would be expected (see Appendix C).

Table 4 provides a list of σ_g values for the worlds considered in this work. With a nominal shear modulus for silicates, ~60 GPa, $Q_t/Q_s \approx 1$ for all these worlds within a few percent. The largest discrepancy by an order of magnitude is the Earth for which $Q_t/Q_s \approx 2/3$.
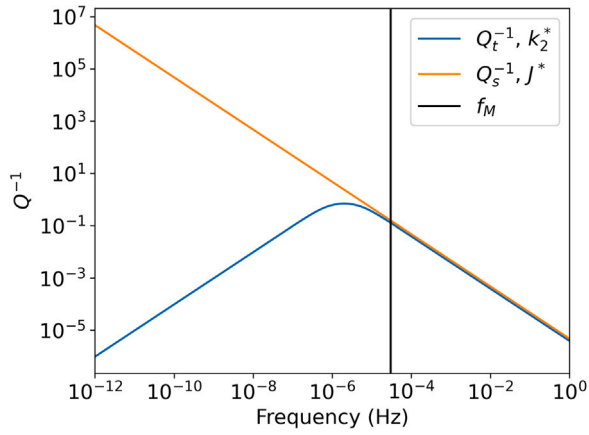
Fig. 2. The tidal and seismic Q^{-1} values have different scaling, but converge at frequencies greater than the Maxwell frequency. For this plot I use the uniform body approximation for k_2 (Eq. (2)), Europa's mass and radius, and a Maxwell rheology of ice ($\eta = 10^{14}$ Pa s, $G_0 = 3$ GPa).

3. The scaling of rheology models to planetary conditions

It is necessarily in planetary tidal heating studies to extrapolate rheology from laboratory conditions (short periods, low viscosity) to planetary conditions (long periods, high viscosity). Therefore it is important to understand the different scaling proposed by the models in Table 2. Fig. 3 shows this scaling for the frequency, viscosity, shear modulus. The nominal parameters in Fig. 3 are chosen to roughly represent Europa's rock mantle as an example (Table 1).

Fig. 3 shows two important products of these rheology models, $-Im(k_2^*)$ (used by tidal heating studies) in the first column and Q_s^{-1} (used in experimental studies) in the second. For most models there is a strong similarity in their scaling to frequency and viscosity, as both strongly impact the viscous term in Eq. (9). Near the Maxwell time (Eq. (11)) the dissipation is maximized for all models. It is also in this region where there is greatest agreement between all the models (with the exception of the β^* model discussed below). At higher viscosity and higher frequency, dissipation drops dramatically for all models, but not at the same rate.

The Maxwell model has the steepest drop in tidal dissipation due to the lack of an anelastic term. This is followed by the Extended Burgers and ζ models which have very similar scaling and would match even closer with slightly different parameter choices. The β and β^* models predict much higher dissipation, however this plot is somewhat misleading for both of these models.

For the case of the β model, as noted in Section 1.2, the controlling β parameter is itself a function of temperature, and therefore would scale with the viscosity of the material in some way. Because of this, the behavior shown in Fig. 3c is artificial to this lack of β scaling.

Of all these models, the behavior of the β^* model is the least well captured by the parameter space exploration of Fig. 3. The β^* model has nearly the same explicit dependence on η as the β model (with viscosity nested in the τ_M term). However the β^* model has another strong temperature and grain-size dependence on the anelastic term with the pseudo-period scaling (Table 2). A more representative scaling for this model would be achieved if one chose a initial material, temperature and grain-size, then forward calculated both viscosity and complex compliance. It is this temperature and material scaling that all these models are attempting to match, but is so embedded into the β^* model that it cannot be easily abstracted back to a pure viscosity scaling.

For all models the scaling with respect to G_0 is minimal. This is because plausible values of the shear modulus simply vary far less than the forcing period or viscosity.

4. Estimating ζ for tidal heating studies

For any application of the widely used Andrade ζ model, a value of ζ must be chosen. Using data from Tan et al. (2001) and Jackson et al. (2002), Castillo-Rogez et al. (2011) argued that a value of $\zeta = 1.0$ is consistent with this experimental data, but did not estimate any uncertainty. The details of this approach are discussed in the following section. Additionally, Efroimsky (2012b) makes theoretical arguments in favor of $\zeta = 1.0$. The thesis of Renaud (2019) reported variation among estimated ζ values but did not attempt to estimate a preferred value.

In this section my goal is to determine the best fit and uncertainty of ζ from the existing experimental data. This will be done in three ways. In Section 4.1 I use a similar approach to Castillo-Rogez et al. (2011) and estimate ζ from other experimentally derived equivalent anelastic quantities (β, n). In Section 4.2 I determine ζ from experimental dissipation values where G_0 and η were independently estimated from strain data. In Section 4.3 I fit the experimental dissipation data directly using a Markov-Chain Monte Carlo approach to estimate ζ. These results will then be compared in Section 4.4.

4.1. Method 1: Estimating values of ζ from experimentally derived anelastic parameters

Comparing the β and ζ versions of the Andrade rheology in Table 2, it can be seen that these controlling parameters are related as follows

$$\beta = \frac{1}{G_0} \zeta^{-n} \left(\frac{\eta}{G_0} \right)^{-n} \tag{29}$$

$$\beta = \zeta^{-n} \eta^{-n} G_0^{n-1} \tag{30}$$

This relationship was also noted by Castillo-Rogez et al. (2011) who then plot the experimentally derived β and $\eta^{-n} G_0^{n-1}$ values. Using data from Tan et al. (2001) and Jackson et al. (2002), they report a linear fit with a slope of 1.02 for the data of Jackson et al. (2002) and 1.03 for the data of Tan et al. (2001). This data is all shown in Fig. 4b. For the same data I get shallower slopes of 0.39 for Tan et al. (2001) and 0.63 for Jackson et al. (2002). I additionally fit the data of Jackson et al. (2004) and find a slope of 0.42. This discrepancy was discussed with the lead author of Castillo-Rogez et al. (2011) but the source of the discrepancy was not found (Castillo-Rogez, 2023, personal communication). Slopes consistent with this work have also been found by Walterová et al. (2023b).

Regardless of this discrepancy, the slope is not the most direct method to estimate ζ from this data. Using Eq. (30), each set of experimentally derived values can be used to form an estimate of ζ. Additionally, errors can be propagated via

$$\sigma_\zeta = \sqrt{\left(\frac{d\zeta}{d\beta} \right)^2 \sigma_\beta^2 + \left(\frac{d\zeta}{d\eta} \right)^2 \sigma_\eta^2 + \left(\frac{d\zeta}{dG_0} \right)^2 \sigma_{G_0}^2 + \left(\frac{d\zeta}{dn} \right)^2 \sigma_n^2} \tag{31}$$

To analyze these in bulk, I treat each estimate as a Gaussian in log-space. This is expressed as

$$p(\zeta) = \frac{1}{\sigma_{\zeta,i}/\zeta_i \sqrt{2\pi}} \exp\left(-\frac{1}{2} \left(\frac{\ln(\zeta) - \ln(\zeta_i)}{\sigma_{\zeta,i}/\zeta_i} \right)^2 \right) \tag{32}$$

where ζ_i is an individual point estimate with error $\sigma_{\zeta,i}$.

As shown in Fig. 4d, these experimental studies result in a broad range of ζ values. The 50-percentile of this summed distribution is at 0.34, slightly higher than the peak of the probability density distribution which is at 0.16. The 16th and 84th percentiles of ζ are at 0.066 and 6.7 respectively. It is important to note that while values of β are clearly temperature dependent, the estimates of ζ are not (Fig. 4c). This is consistent with the argument that the form of the Andrade ζ model is capturing at least the majority of that temperature dependence, but does not rule out a more subtle temperature as suggested by Renaud (2019).
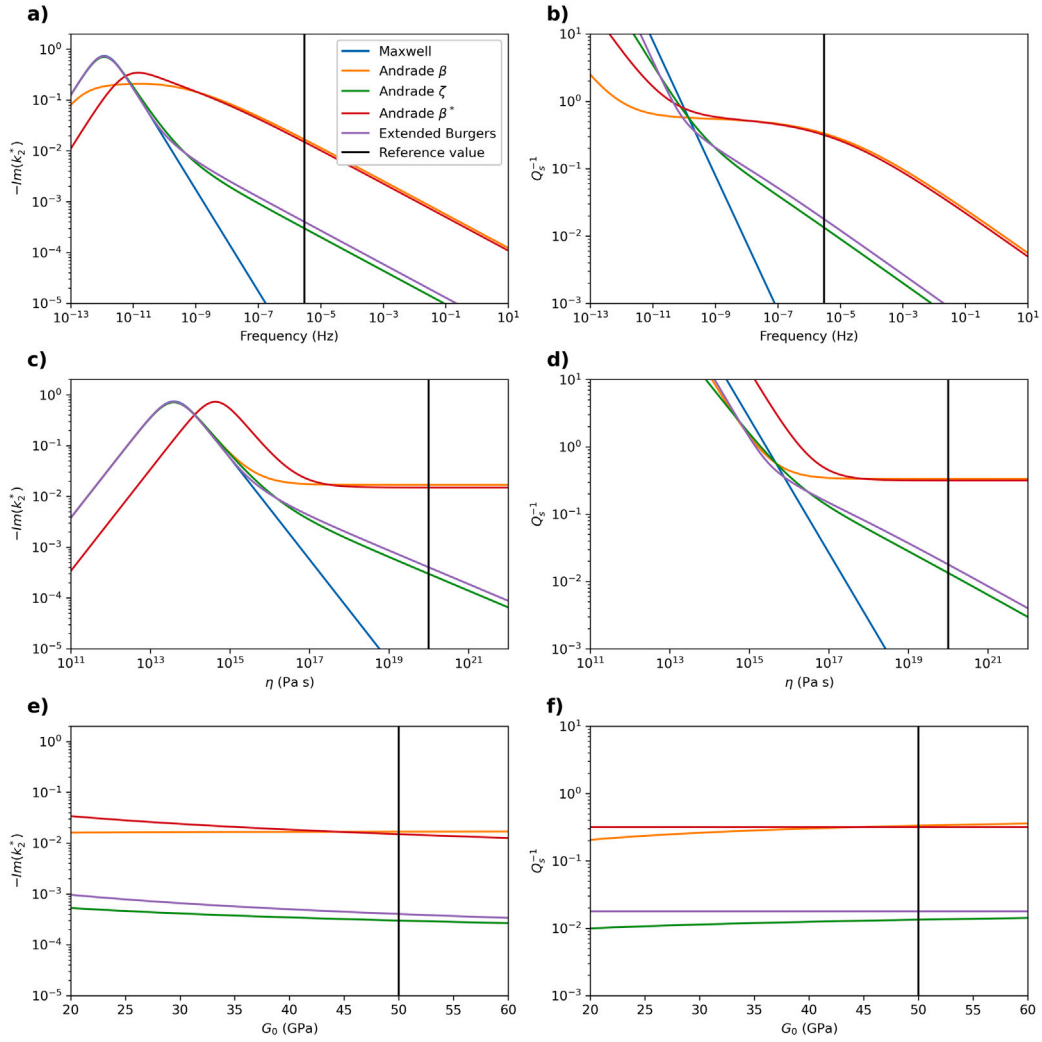
Fig. 3. The rheology models in Table 2 make orders of magnitude different predictions for the tidal heating in a Europa like planetary mantle due to the scaling with forcing period and viscosity. The first column (panels a,c,e) show $-Im(k_2)$ for an assumed uniform body (Eq. (2)). This scales directly with the expected tidal dissipation (Eq. (1)). The second column (panels b,d,f) shows the seismic Q_s^{-1} for the same parameters (see Section 2). The vertical black line in each panel shows the reference value used in all other panels (given in Table 1).

4.2. Method 2: Estimating ζ from studies with independent η and G_0

The Andrade ζ model has four unknown parameters (G_0, η, ζ, n) that are used to estimate two outcomes (G, Q^{-1}). In this subsection I show how, for cases where G_0 and η are independently estimated from strain rate data, each measurement pair of G and Q_s^{-1} can be used to estimate values of ζ and n. For this section I use data from Takei et al. (2014) and Yamauchi and Takei (2016) as they both directly estimate viscosity directly from the strain rate data for their samples at every temperature.

First I will show how J_1 and J_2 can be directly estimated from Q_s^{-1} and G

$$Q_s^{-1} = \frac{J_2}{J_1} \tag{33}$$

$$G = \left[\sqrt{J_1^2 + J_2^2} \right]^{-1} \tag{34}$$

$$G = \left[\sqrt{J_1^2 + (J_1 Q_s^{-1})^2} \right]^{-1} \tag{35}$$

$$G^{-2} = J_1^2 \left(1 + (Q_s^{-1})^2 \right) \tag{36}$$

For this it is useful to write the Andrade ζ model as

$$J_1 = \frac{1}{G_0} + \frac{1}{G_0} \left(\zeta \frac{\eta}{G_0} \omega \right)^{-n} \Gamma(n+1) \cos\left(\frac{n\pi}{2}\right) \tag{37}$$

$$J_2 = \frac{1}{\eta\omega} + \frac{1}{G_0} \left(\zeta \frac{\eta}{G_0} \omega \right)^{-n} \Gamma(n+1) \sin\left(\frac{n\pi}{2}\right) \tag{38}$$

Keeping only the anelastic terms on the right hand side of the equations, I divide these equations to get

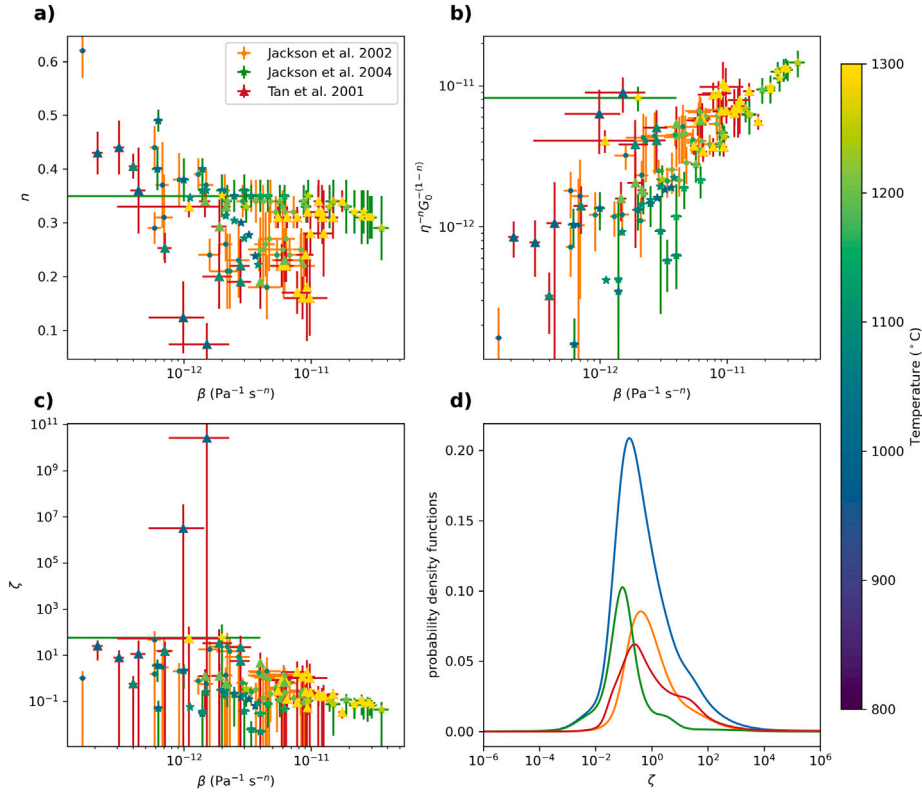$$\frac{J_2 - \frac{1}{\eta\omega}}{J_1 - \frac{1}{G_0}} = \tan\left(\frac{n\pi}{2}\right) \tag{39}$$

$$n = \frac{2}{\pi} \arctan\left(\frac{J_2 - \frac{1}{\eta\omega}}{J_1 - \frac{1}{G_0}} \right) \tag{40}$$

I than then solve both Eqs. (37) and (38) for ζ and get

$$\zeta^n = \frac{\Gamma(n+1) \cos\left(\frac{n\pi}{2}\right)}{G_0 \left(J_1 - \frac{1}{G_0} \right) \left(\frac{\eta}{G_0}\omega \right)^n} \tag{41}$$

$$\zeta^n = \frac{\Gamma(n+1) \sin\left(\frac{n\pi}{2}\right)}{G_0 \left(J_2 - \frac{1}{\eta\omega} \right) \left(\frac{\eta}{G_0}\omega \right)^n} \tag{42}$$

If for a given data point, n is solved for with Eq. (40), Eqs. (41) and (42) will produce identical results. However if one assumes the value of n independent of Eq. (40) (eg. assuming a common value of $1/3$ or the

Fig. 4. Values of ζ extracted from experimentally derived β, n, G_0, and η imply a broad range of values between 0.06 to 6. (a) Values of β and n. The symbol shape and color of error bars indicate the study the value is from. Symbol colors indicate the temperature of the experiment. All values are for poly-crystalline olivine. (b) Experimental quantities of Eq. (30) plotted in a similar fashion to Figure 4 in Castillo-Rogez et al. (2011). (c) Values of ζ derived from the values in panel b and Eq. (30). (d) Summation of ζ estimates, treating each as a Gaussian (Eq. (32)). For reference each study has the following number of derived values: Tan et al. (2001) $N = 35$, Jackson et al. (2002) $N = 38$, Jackson et al. (2004) $N = 33$.
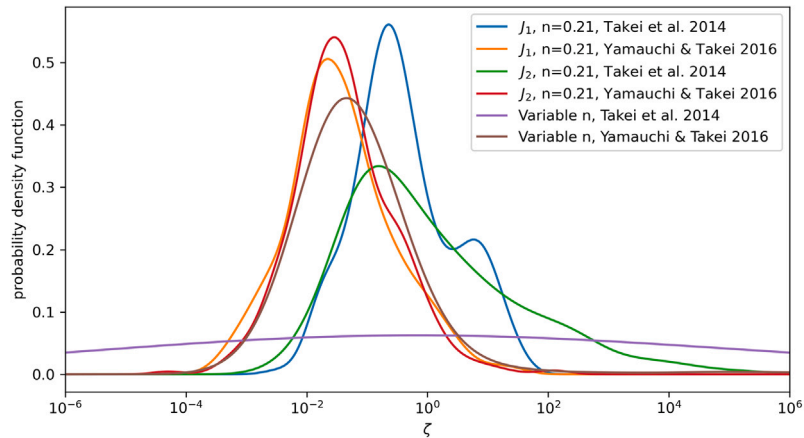
Fig. 5. Direct fitting of boreal data with independently measured G_0 and η finds values ζ between $10^{-3} - 10^{1}$. The probability density estimate of $\log_{10}(\zeta)$ is determined by Gaussian kernel density estimation with a bandwidth of 0.3.

median value of the dataset), Eqs. (41) and (42) may produce slightly different estimates.

The ζ estimates obtained through this approach are shown in Fig. 5. Using data from Takei et al. (2014) and Yamauchi and Takei (2016) the median value of n is 0.21 (solved using Eq. (40)). When using the unique n value associated with each data point the data of Yamauchi and Takei (2016) peaks at $\zeta = 0.05$ with 16th and 84th percentile values of 0.02 and 0.3. For the data of Takei et al. (2014) the median is similarly $\zeta = 0.4$ but outliers pull the 16th and 84th percentile values to 0.07 and 3×10^7 respectively. These outliers are discussed in more detail in Appendix D. Also shown in Fig. 5 are the values determined

with a fixed $n = 0.21$ using Eqs. (41) and (42). These approached all lead to ζ estimates between $10^{-3} - 10^{1}$.

4.3. Method 3: Fitting ζ with MCMC

The last approach used to determining ζ from the existing experimental data is to fit the ζ model to the experimentally observed G and Q_s^{-1} values directly. This was done for data sets where neither of the above approaches could be performed (because the required parameters were either not estimated or not reported). I performed this fitting using a Markov-Chain Monte Carlo (MCMC) procedure.
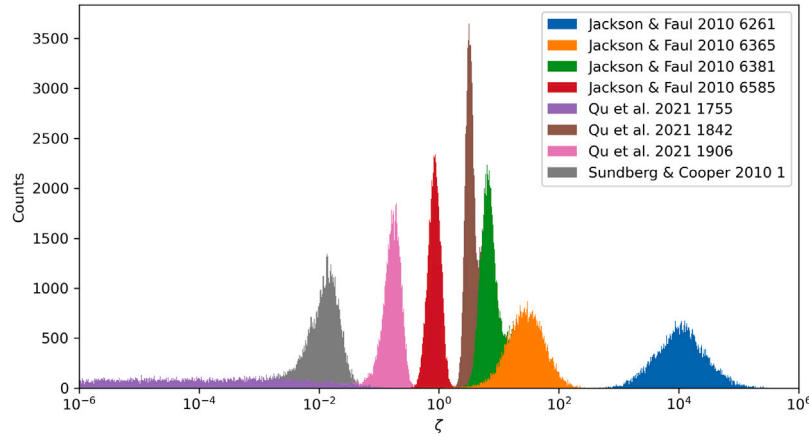
Fig. 6. MCMC estimations of ζ vary by many orders of magnitude between samples with most values between $10^{-2} - 10^2$. This figure shows a histogram of the last 50,000 MCMC samples (of 3 million) for each sample fit.

Very generally, MCMC is a method of curve fitting wherein the fitting parameters are varied randomly and those variations are accepted or rejected depending on if they improve the fit to the data. For this work the MCMC approach was implemented using the python EMCEE package (Foreman-Mackey et al., 2013).

I only used samples where data was available across a wide range of temperatures for the same sample to break some of the degeneracies that arise in this fitting. For this, olivine samples from Jackson and Faul (2010), Sundberg and Cooper (2010), and olivine-pyroxene samples from Qu et al. (2021) where used with this approach. Only measurements at temperatures above 800 °C were used in the fitting to avoid regimes where grain boundary sliding was not the dominant deformation mechanism.

Because in this approach I am fitting G and Q_s^{-1} values across all temperatures and frequencies simultaneously, I must use an assumed temperature dependence for G_0 and η. For the unrelaxed shear modulus I assume it linearly drops with temperature from some reference value, G_{0R}, at a reference temperature, T_R, at a constant rate of $\frac{dG}{dT}$. This is the same scaling used by Jackson and Faul (2010) and is given by

$$G_0 = G_{0R} + \frac{dG}{dT}(T - T_R) \tag{43}$$

For the viscosity I assume a Newtonian viscosity with an Arrhenius temperature scaling from a reference value of η_R and an activation energy of E_η.

$$\eta = \eta_R \exp\left(\frac{E_\eta}{R}\left[\frac{1}{T} - \frac{1}{T_R}\right]\right) \tag{44}$$

In total there are six free parameters being fit, ζ, n, G_{0R}, dG/dT, η_R, E_η. With these, J^* is calculated using the Andrade ζ model (Table 2) and Q_s^{-1} and G are calculated (Eqs. (7) and (8). The natural log of the likelihood function is then calculated as

$$\ln(p) = -\frac{1}{2}\sum_n\left[\left(\frac{G_i - G_{obs}}{G_{obs} * 0.03}\right)^2 + \left(\frac{\log_{10}(Q_i^{-1}) - \log_{10}(Q_{obs}^{-1})}{0.05}\right)^2\right] \tag{45}$$

The use of $G_{obs} * 0.03$ as the error in G_{obs} and 0.05 as the error in the $\log_{10}(Q_{obs}^{-1})$ are the values and forms suggested by Jackson and Faul (2010).

All six of the free parameters have a uniform prior probability. The full parameter bounds used and all the resulting parameter estimations are presented in Appendix A. The parameters ζ and η_R were varied in log-space. The parameter space was sampled by thirty walkers each taking one hundred-thousand steps. Convergence was estimated using fifty times the auto-correlation time of the sample chains. The longest estimated convergence time in this dataset is ~21000 steps. Every solution corner plot and comparison the data are presented in the Supplemental Figures S1–S16.

This MCMC fitting to samples directly results in a very wide range of ζ values (Fig. 6 and Table A.7). Most of the sample values lie between 10^{-2} and 10^2. There are two outliers from this range.

Sample 6261 from Jackson and Faul (2010) has a peak around at $\zeta = 10^4$. This sample has less data points being fit (33 measurements compared to ~50 for 6585 and 6381) and none of those measures were at periods above 100 s where the anelastic effects become more significant. In the data for sample 6261 the shear modulus slightly rises between 800 °C and 900 °C. This kind of behavior cannot be captured in the Andrade creep model, which may drive the fitting to unrealistic values. This sample also has a very low estimate of $n = 0.14$. The corner plot in Figure S5 shows that if n was constrained to a higher value, the estimate of ζ would be orders of magnitude lower.

The other outlier is Sample 1755 from Qu et al. (2021). For this sample the only constraint is that $\zeta \leq 10^{-2}$ with a very strong degeneracy between ζ and η present (Figure S9). It may be the lack of measurements above 1200 °C that leads to the weaker constraint on η when compared to the other samples from Qu et al. (2021).

Several of the samples do have poorly fit viscosity values in these inversions, where the uncertainty in the reference viscosity spans several orders of magnitude. This is particularly true for samples 6365 (Jackson and Faul, 2010), 1755 (Qu et al., 2021) and 1906 (Qu et al., 2021) (see figures S3, S9, S13). This is likely due to a combination of factors. First, in the attenuation data fit here you cannot directly separate transient vs. steady state deformation (as can be done more directly with strain rate data). Second, fits to the attenuation data are less sensitive to viscosity for very large values of viscosity as the viscous component of the complex compliance goes to zero. For these reasons, viscosity estimated from the strain rate data directly, as was done for the samples used in Section 4.2, are more reliable. However the best constrained outliers in this inversion for ζ, samples 6261 (Jackson and Faul, 2010) and the data from Sundberg and Cooper (2010), do have well constrained viscosity distributions (Figures S5 and S15). Only for sample 1755 (Qu et al., 2021) does the uncertainty in viscosity directly lead to a large uncertainty in ζ.

4.4. Summary of ζ results

In this Section 1 compare the resulting ζ values from the methods of the previous three sections. The percentiles estimates of ζ for each approach are given in Table 5. These three methods each only broadly similar results. The median (50th percentile) value across the three runs varies from 0.09 to 1.7, over an order of magnitude spread. The 1-sigma variations (16th to 84th percentiles) are roughly 10^{-2} to 10. None of the three methods strongly constrain the 5th or 95th percentile values and as such these vary dramatically between the three methods. The

Table 5
From all methods the preferred values of zeta range from roughly 10^{-2} to 10 with a median value around 10^{-1}. The 5th and 95th percentiles are far less consistent due to the limited data in all approaches. For method 2 the percentiles shown are calculated with Eq. (41) and the median n value of 0.21.

Method	Percentile				
	5	16	50	84	95
Method 1: Using anelastic parameters	0.019	0.061	0.35	6.7	110
Method 2: Using independent η and G_0	2.5×10^{-3}	0.011	0.086	0.87	7.2
Method 3: MCMC	9.0×10^{-7}	0.0095	1.7	38	1.4×10^4
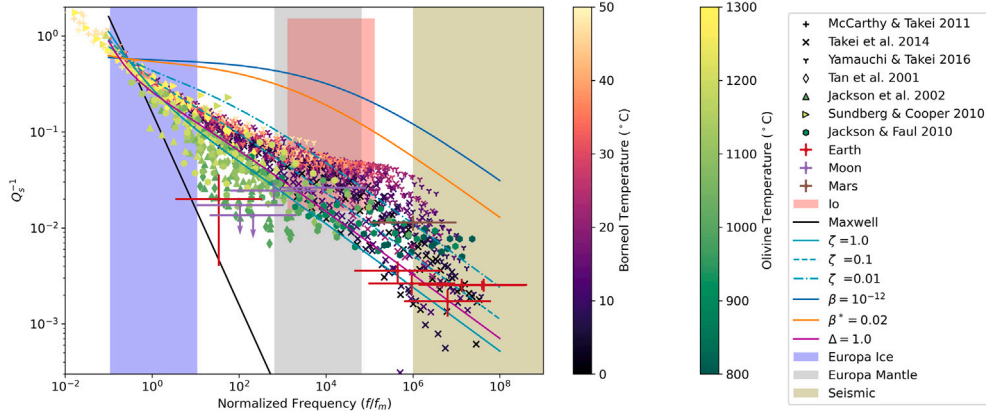
Fig. 7. The Extended Burgers and ζ Andrade models are the most consistent with the experimental studies and planetary Q values when re-scaled by the Maxwell frequency. All data points are the same as those shown in Fig. 1. Experimental values are normalized using G_0 and η values reported with the data. Planetary values are normalized assuming $G_0 = 50$ GPa and a range of viscosity from 10^{19} Pa s to 10^{21}. Io's $|k_2^*|/Q_t$ is converted to Q_t^{-1} assuming $|k_2^*|$ is in the range 0.01 to 1.0 (Bierson and Nimmo, 2016).

commonly used value of $\zeta = 1$ is well within the 1-sigma variation of the results presented here, although it is not preferred over a much smaller value of 0.1.

5. Universal scaling of Q and rheology models

McCarthy et al. (2011) have previously suggested that attenuation in all polycrystalline materials in the grain-boundary sliding deformation regime follow the same trend when scaled by their Maxwell time. Fig. 7 applies this idea not only to a broad range of the available lab studies (Section 1.3), but also to the rheology models (Section 1.2) and planetary Q estimates (Section 1.4). These are the same values presented in Fig. 1, with this Maxwell time normalization.

Also shown on this figure is the range of normalized frequencies that would be expected for Europa's ice shell (blue shading) and mantle (gray shading). With this normalization, the regimes expected for Europa's ice shell and mantle are actually very well sampled by the existing experimental literature. In this space, Europa's ice shell sits near the Maxwell frequency where all the rheology models converge. Europa's mantle is in the region dominated by anelastic behavior, and therefore, the region of largest discrepancy between rheology models.

Experimental values from Yamauchi and Takei (2016) include some melt and generally fall above the melt free comparable samples of Takei et al. (2014). The melt bearing samples of Jackson et al. (2004) (not shown) also plot above the melt free comparable samples of Tan et al. (2001) and Jackson et al. (2002).

In Fig. 7, the Maxwell rheology underestimates the dissipation for nearly all the experimental data. Conversely, the constant β and pseudo-period β^* models overestimate the dissipation. If a far lower viscosity is used (closer to $\eta = 10^{11}$ Pa s) the Andrade β and β^* models will fall more in line with the normalized data, consistent with McCarthy and Cooper (2016). The ζ and Extended Burgers models lie within the experimental data regardless of the chosen viscosity.

In this space it can also be seen that the planetary Q values measured for the Earth, Moon, and Mars (Table 3) are broadly consistent with the experimental data. All the planetary and experimental values

are in the regime $f/f_M > 1.0$ where it is expected $Q_t^{-1} \approx Q_s^{-1}$ (Section 2). The values that deviate the most from the experimental data are those from the Earth and Moon with the lowest f/f_M. The consistency between planetary and laboratory values is in spite of the ten (or more for the Boreal data) orders of magnitude difference in viscosity, validating the underlying theory.

6. Discussion

The broader range of ζ values implied by this work has important implications for the amount to tidal heating expected in the silicate mantle of worlds like Europa. As an example, Běhounková et al. (2021) found tidal heating could drive some volcanism in Europa's mantle with a model that assumed $\zeta = 1.0$. Applying the uniform body approximation (Eq. (2)), it would be expected that with $\zeta = 10^{-2}$, there would be ~5 times more heating in the mantle (than for $\zeta = 1.0$). That would change tidal heating from being less than radiogenic heating, to being more than double the radiogenic heating. This would in turn impact both the expected conditions at Europa's seafloor as well as the orbital evolution (Hussmann and Spohn, 2004).

For the application of tidal heating, I do recommend using either the ζ or Extended Burgers models. However I am not saying that the β or β^* models are intrinsically less correct. Tidal heating studies typically treat viscosity as the key free parameter of the material. In the β model there is no clearly established scaling for how the parameter β changes with viscosity (this is the purpose of the ζ model). For the β^* model, the pseudo-period scaling is given as function of grain-size and temperature. One could chose a temperature and grain-size, then forward calculate viscosity and the pseudo-period separately. This approach may adjust the β^* curve in Fig. 7 to be more in line with the data.

The comparison of planetary Q_t^{-1} values to experimental Q_s^{-1} samples in 7 is not meant to imply that these quantities are entirely equivalent, but to show their close connection. The approximation $Q_t^{-1} \approx Q_s^{-1}$ (Section 2) assumes that the planetary bodies are uniform. This may be part of the reason that the low frequency tidal Q_t^{-1} for

the Earth and moon fall below the trend of experimental values. While experimental samples are manufactured to be uniform, worlds have interior gradients in temperature, composition, and stress. Recent work has demonstrated the importance of these considerations for the lunar Q_t^{-1} values (Xiao et al., 2022; Walterová et al., 2023a). Fig. 7 still shows that, at least to first order, the planetary Q_t^{-1} values are consistent with the laboratory Q_s^{-1}. This strengthens the arguments of McCarthy et al. (2011) that there is a universal behavior to the dissipation in polycrystalline materials, without disputing the importance of considering deviations from that trend (Jackson et al., 2014; Faul and Jackson, 2015).

One question that arises from this work, is what new experiments would be most instructive for constraining these tidal heating studies. The problem with simply extending to lower frequencies (as might be suggested from Fig. 1) is that you would begin measuring dissipation on the viscous side of the Maxwell peak ($f/f_M < 1.0$). This regime may be relevant for the warmest parts of Europa's ice shell, but not general planetary mantles. For tidal heating studies in-particular, studies which directly estimate values of ζ, and the associated uncertainty, would be of particular value. Despite being widely used, at this point estimates of ζ only come from secondary analysis of laboratory data (Castillo-Rogez et al., 2011; Walterová et al., 2023b). This approach is inherently limited as the raw time-domain strain data is rarely available for such secondary analysis. I suspect that laboratory work with an explicit aim of constraining ζ could produce stronger constraints than have been reported in this work.

In Table 2, I list three different rheology models that are all referred to as "Andrade" in the literature. In Section 3 I show that these three models all have different scaling to important parameters because of their construction. Because of this ambiguity in the term "Andrade" it is extremely important for all tidal heating studies to explicitly describe the complex compliance of their rheology model.

7. Conclusions

Extrapolation from lab scale experiments to planetary mantles requires orders of magnitude changes in grain-size, viscosity, and forcing period. Additionally, many of the existing rheological models have been designed for explaining seismic observations. The types of parameter space exploration used in seismic studies and planetary tidal heating applications often differ. Using a Maxwell normalized frequency I compared the laboratory data, planetary Q values, and rheological models. I find that the Andrade ζ model and Extended Burgers models are both consistent with all these data sets. I also find that a wide range of ζ values should be explored to encompass the uncertainty seen in experimental studies. This uncertainty would generally push models towards predicting more dissipation in planetary mantles.

CRediT authorship contribution statement

Carver J. Bierson: Writing – review & editing, Writing – original draft, Visualization, Validation, Software, Project administration, Methodology, Investigation, Formal analysis, Data curation, Conceptualization.

Declaration of competing interest

The authors declare that they have no known competing financial interests or personal relationships that could have appeared to influence the work reported in this paper.

Data availability

No experimental data was produced for this work. Data produced in the MCMC fitting is available at the Zenodo directory https://doi.org/10.5281/zenodo.10264836.

Table A.6
Bounds used for fitting the Andrade ζ model.

	Lower bound	Upper bound
ζ	10^{-9}	10^9
n	0.05	0.9
G_{0R}	10 GPa	100 GPa
dG/dT	−300 MPa/K	0
η_R	10^5 Pa s	10^{30} Pa s
E_η	10 J mol^{-1} K^{-1}	10^7 J mol^{-1} K^{-1}

Appendix A. Detailed methods for determining ζ via MCMC

This appendix provides some more details of the Markov-Chain Monte Carlo (MCMC) method used to determine ζ (results in Section 4.3). The errors presented in Table A.7 are taken from the distributions of all points after 50 auto-correlation times have passed. The longest auto-correlation time in this data set was 432 steps, implying convergence after ~21000 steps. The extremely large number of steps taken is done to make sure no memory of the initial conditions are present. All parameters have a uniform prior probability distribution with bounds given in Table A.6.

The resulting model fits are presented in Table A.7. Normalized chi-squared values for the best fit values are also given and can be compared with the original fits to the experimental papers. The distribution of all MCMC fits is shown in the main text Fig. 6. The corner plots and data fits for all samples used are presented in the supplemental information.

Appendix B. Extended Burgers model values

Here I briefly apply the statistical method of Section 4.1 to literature values of the Burgers parameter Δ. The values used are shown in Fig. B.8. The 50-percentile of this summed distribution is at 0.85, slightly lower than the peak of the probably density distribution which is at 1.3. The 16th and 84th percentiles of ζ are at 0.22 and 1.8 respectively.

Appendix C. Deriving peak heating in a Maxwell rheology

In this appendix I derive the frequency of peak tidal heating for a Maxwell Rheology. I begin with the imaginary part of k_2^* as given by Renaud and Henning (2018)

$$-Im(k_2^*) = \frac{3}{2} \frac{\tau_M 2\pi f G_0/\sigma_g}{1 + (\tau_M 2\pi f)^2 (G_0/\sigma_g + 1)} \tag{C.1}$$

To find the peak I will take the derivative with respect to frequency and set it to zero.

$$\frac{d(-Im(k_2^*))}{df} = \frac{3}{2} \frac{\tau_M 2\pi G_0/\sigma_g - (\tau_M 2\pi)^3 G_0/\sigma_g (G_0/\sigma_g + 1) f^2}{\left(1 + (\tau_M 2\pi f)^2 (G_0/\sigma_g + 1)\right)^2} \tag{C.2}$$

$$\frac{d(-Im(k_2^*))}{df} = 0 \tag{C.3}$$

$$\tau_M 2\pi G_0/\sigma_g - (\tau_M 2\pi)^3 G_0/\sigma_g (G_0/\sigma_g + 1) f_{peak}^2 = 0 \tag{C.4}$$

$$f_{peak}^2 = \frac{1}{(\tau_M 2\pi)^2 (G_0/\sigma_g + 1)} \tag{C.5}$$

$$f_{peak} = \frac{1}{(\tau_M 2\pi) \sqrt{G_0/\sigma_g + 1}} \tag{C.6}$$

Table A.7

Values fit via MCMC to the data from Jackson and Faul (2010), Sundberg and Cooper (2010), Qu et al. (2021) assuming an Andrade ζ model. Grain size is not used or fit by the model but is shown for reference. Errors are the distance to the 16th and 84th percentiles. Distributions of ζ values are shown in Fig. 6.

Sample	Grain size (μm)	ζ	n	G_{0R} (GPa)	$\frac{dG}{dT}$ (MPa/K)	$\log_{10} \eta_R$ (Pa s)	E_η (kJ/mol)	$\left(\chi^2/2N\right)$
6585 (J10)	3.1	0.8 ± 0.2	0.330 ± 0.008	62.7 ± 0.5	-18 ± 3	15.9 ± 0.1	296 ± 8	0.94
6365 (J10)	12.4	28^{+25}_{-14}	0.22 ± 0.02	65.0 ± 0.5	-17 ± 3	16.2 ± 0.2	320 ± 20	1.09
6261 (J10)	23.4	$(1.0^{+1.6}_{-0.6}) \times 10^4$	0.14 ± 0.01	65.3 ± 0.5	-17 ± 3	16.2 ± 0.3	350 ± 30	1.32
6381 (J10)	2.9	6 ± 2	0.24 ± 0.01	63.1 ± 0.04	-24 ± 2	16.2 ± 0.01	364 ± 13	1.35
1755 (Q21)	3.1	$5 \times 10^{-6}\ {}^{+1.7\times10^{-3}}_{-5.0\times10^{-6}}$	0.40 ± 0.006	61 ± 0.2	21 ± 1.4	21.6 ± 2.5	300 ± 5	5.06
1842 (Q21)	3.0	$3.23^{+0.54}_{-0.47}$	0.16 ± 0.005	68.1 ± 0.3	-9.3 ± 2	19.5 ± 1.8	573 ± 17	2.48
1906 (Q21)	7.5	0.16 ± 0.005	0.31 ± 0.007	65.7 ± 3.8	-25 ± 2	19.5 ± 0.16	518 ± 11	3.16
SC10	5	0.013 ± 0.007	0.24 ± 0.02	66 ± 9	-22 ± 18	18.6 ± 0.3	646 ± 23	1.25
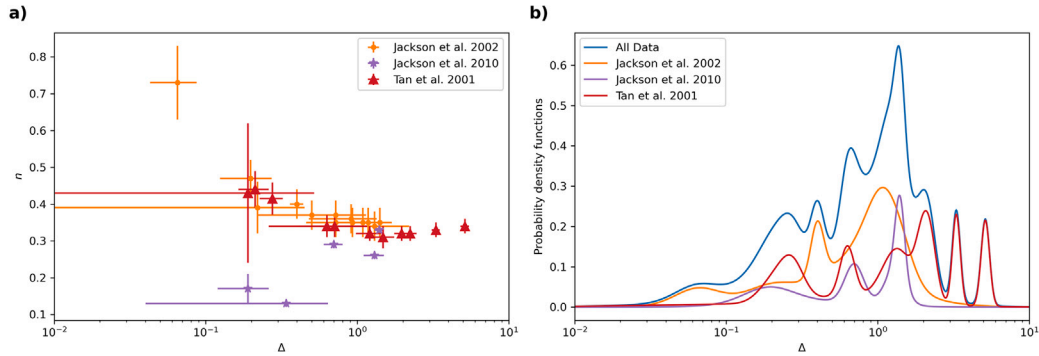
Fig. B.8. Burgers fits from Tan et al. (2001), Jackson et al. (2002), Jackson and Faul (2010). (a) individual data points from each study. (b) Δ probability density functions following the same method presented in Section 4.1 for ζ.
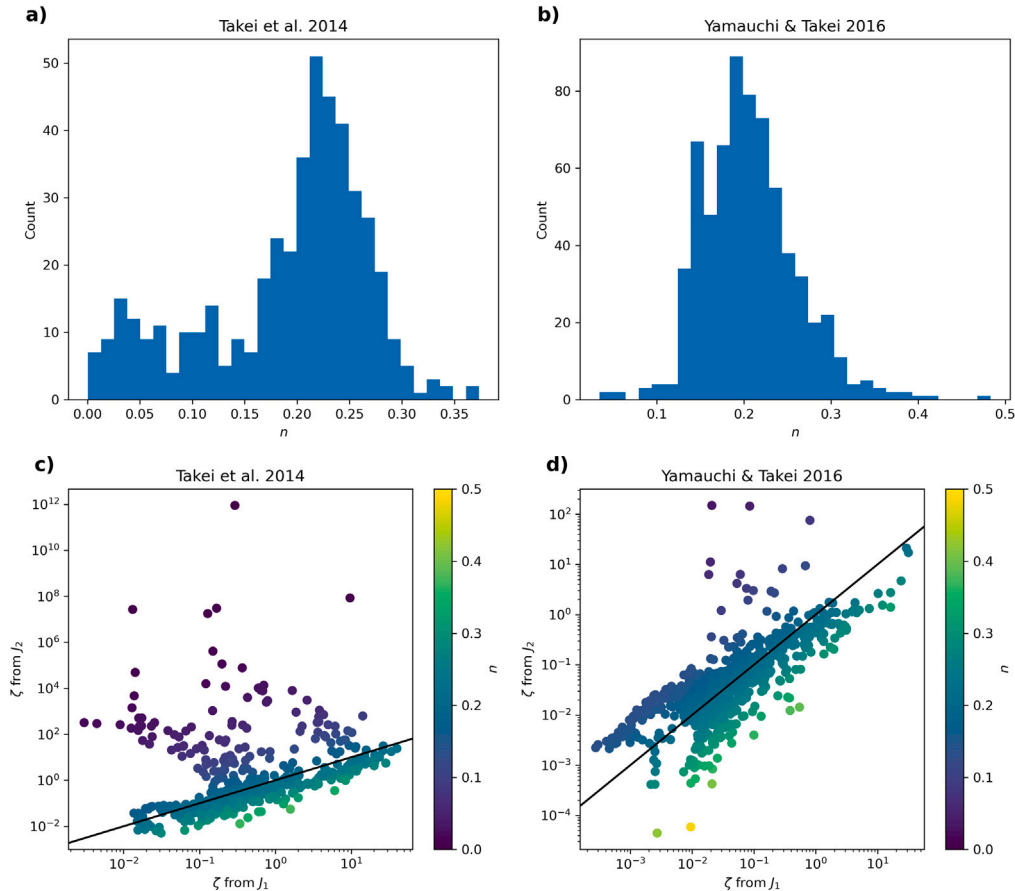
Fig. D.9. More detailed parameter estimation results using the methods of Section 4.2. Panels a and b show estimates of n derived from Eq. (40). Panels c and d show estimates of ζ derived from J_1 using Eq. (41) (x-axis) or J_2 using Eq. (42) (y-axis).

$$\frac{f_{peak}}{f_M} = \frac{1}{(2\pi)\sqrt{G_0/\sigma_g + 1}} \tag{C.7}$$

For the Example Europa case in Fig. 2, $\frac{f_{peak}}{f_M} \approx 0.067$. For most common values of G_0 and σ_g the peak Maxwell dissipation will occur a frequency 10–20 times lower than the Maxwell frequency.

Appendix D. Details of ζ fitting with known η and G_0

This appendix describe more detail of the ζ estimation described in Section 4.2, and particularly the outliers in that dataset. Panels a and b of Fig. D.9 show histograms of all n values estimated via Eq. (40). The median values of n are 0.21 for Takei et al. (2014) and 0.20 for Yamauchi and Takei (2016). However in the data of Takei et al. (2014) there is also a peak of values a $n < 0.1$.

Panels c and d of Fig. D.9 compare values of ζ calculated using either J_1 using Eq. (41) (x-axis) or J_2 using Eq. (42) (y-axis). In both cases a fixed value of $n = 0.21$ is used. The black line is a 1–1 line that would be expected if n was constant across the dataset.

Of note, for the data of Takei et al. (2014), the same samples for which $n < 0.1$ (from Eq. (40)) the value of ζ estimated from J_2 (Eq. (42)) are many orders of magnitude larger than those estimated using J_1 (Eq. (41)) and many orders of magnitude larger than is expected generally. These samples are also some of the lowest temperature samples in the dataset of Takei et al. (2014). Eq. (42) is much more sensitive to η than Eq. (41). I speculate that errors in the viscosity estimation for these lowest temperature samples are the cause of this difference.

Regardless of the underlying cause, the greater consistency of Eq. (41) is the reason it is used for the values presented in Table 5.

Appendix E. Supplementary data

Supplementary material related to this article can be found online at https://doi.org/10.1016/j.icarus.2024.116026.

References

Abrahams, J., 2022. Planetary Heat: Exploring how Planetary Surfaces are Shaped (Ph.D. thesis). University of California Santa Cruz.

Anderson, J.D., Jacobson, R.a., Lau, E.L., Moore, W.B., Schubert, G., 2001. Io's gravity field and interior structure. J. Geophys. Res. 106 (E12), 32963. http://dx.doi.org/10.1029/2000JE001367.

Andrade, E.N.d.C., 1910. On the viscous flow in metals, and allied phenomena. Proc. R. Soc. Lond. Ser. A Contain. Pap. Math. Phys. Character 84 (567), pp. 1–12, URL http://www.jstor.org/stable/92859.

Bagheri, A., Khan, A., Al-Attar, D., Crawford, O., Giardini, D., 2019. Tidal response of mars constrained from laboratory-based viscoelastic dissipation models and geophysical data. J. Geophys. Res: Planets 124 (11), 2703–2727. http://dx.doi.org/10.1029/2019JE006015, URL https://onlinelibrary.wiley.com/doi/abs/10.1029/2019JE006015.

Barnhoorn, A., Jackson, I., Fitz Gerald, J.D., Kishimoto, A., Itatani, K., 2016. Grain size-sensitive viscoelastic relaxation and seismic properties of polycrystalline MgO. J. Geophys. Res.: Solid Earth 121 (7), 4955–4976. http://dx.doi.org/10.1002/2016JB013126, arXiv:https://agupubs.onlinelibrary.wiley.com/doi/pdf/10.1002/2016JB013126.

Behn, M.D., Hirth, G., Elsenbeck, J.R., 2009. Implications of grain size evolution on the seismic structure of the oceanic upper mantle. Earth Planet. Sci. Lett. 282 (1), 178–189. http://dx.doi.org/10.1016/j.epsl.2009.03.014, URL https://www.sciencedirect.com/science/article/pii/S0012821X09001575.

Benjamin, D., Wahr, J., Ray, R.D., Egbert, G.D., Desai, S.D., 2006. Constraints on mantle anelasticity from geodetic observations, and implications for the J2 anomaly. Geophys. J. Int. 165 (1), 3–16. http://dx.doi.org/10.1111/j.1365-246X.2006.02915.x.

Bierson, C.J., Nimmo, F., 2016. A test for Io's magma ocean: Modeling tidal dissipation with a partially molten mantle. J. Geophys. Res: Planets 121 (11), 2211–2224. http://dx.doi.org/10.1002/2016JE005005, 2016JE005005.

Bills, B.G., Neumann, G.a., Smith, D.E., Zuber, M.T., 2005. Improved estimate of tidal dissipation within mars from MOLA observations of the shadow of Phobos. J. Geophys. Res. E: Planets 110 (7), 1–15. http://dx.doi.org/10.1029/2004JE002376.

Běhounková, M., Tobie, G., Choblet, G., Kervazo, M., Melwani Daswani, M., Dumoulin, C., Vance, S.D., 2021. Tidally induced magmatic pulses on the oceanic floor of Jupiter's moon Europa. Geophys. Res. Lett. 48 (3), http://dx.doi.org/10.1029/2020GL090077, e2020GL090077. URL https://onlinelibrary.wiley.com/doi/abs/10.1029/2020GL090077.

Castillo-Rogez, J., 2023. Personal communication.

Castillo-Rogez, J.C., Efroimsky, M., Lainey, V., 2011. The tidal history of Iapetus: Spin dynamics in the light of a refined dissipation model. J. Geophys. Res: Planets 116 (E9), n/a–n/a. http://dx.doi.org/10.1029/2010JE003664, E09008.

Cathles, L.M., 1975. Viscosity of the Earth's Mantle. Princeton University Press.

Efroimsky, M., 2012a. Bodily tides near spin–orbit resonances. Celestial Mech. Dynam. Astronom. 112 (3), 283–330. http://dx.doi.org/10.1007/s10569-011-9397-4.

Efroimsky, M., 2012b. Tidal dissipation compared to seismic dissipation: In small bodies, earths, and super-earths. Astrophys. J. 746 (2), 150, URL http://stacks.iop.org/0004-637X/746/i=2/a=150.

Faul, U.H., Jackson, I., 2005. The seismological signature of temperature and grain size variations in the upper mantle. Earth Planet. Sci. Lett. 234 (1), 119–134. http://dx.doi.org/10.1016/j.epsl.2005.02.008, URL https://www.sciencedirect.com/science/article/pii/S0012821X05001044.

Faul, U., Jackson, I., 2015. Transient creep and strain energy dissipation: An experimental perspective. Ann. Rev. Earth Planet. Sci. 43 (1), 541–569. http://dx.doi.org/10.1146/annurev-earth-060313-054732.

Findley, W.N., Lai, J.S., Onaran, K., 1976. Creep and Relaxation of Nonlinear Viscoelastic Materials With an Introduction to Linear Viscoelasticity. Dover, http://dx.doi.org/10.1115/1.3424077.

Foreman-Mackey, D., Hogg, D.W., Lang, D., Goodman, J., 2013. Emcee: The MCMC hammer. Publ. Astron. Soc. Pac. 125 (925), 306. http://dx.doi.org/10.1086/670067, arXiv:1202.3665.

Gevorgyan, Y., Boué, G., Ragazzo, C., Ruiz, L.S., Correia, A.C.M., 2020. Andrade rheology in time-domain. application to Enceladus' dissipation of energy due to forced libration. Icarus 343, 113610. http://dx.doi.org/10.1016/j.icarus.2019.113610, URL https://www.sciencedirect.com/science/article/pii/S0019103519305020.

Goldreich, P., Gold, T., 1963. On the eccentricity of satellite orbits in the solar system. Mon. Not. R. Astron. Soc. 126 (3), 257–268. http://dx.doi.org/10.1093/mnras/126.3.257, arXiv:https://academic.oup.com/mnras/article-pdf/126/3/257/8074961/mnras126-0257.pdf.

Gribb, T.T., Cooper, R.F., 1998. Low-frequency shear attenuation in polycrystalline Olivine: Grain boundary diffusion and the physical significance of the Andrade model for viscoelastic rheology. J. Geophys. Res.: Solid Earth 103 (B11), 27267–27279. http://dx.doi.org/10.1029/98JB02786.

Hussmann, H., Spohn, T., 2004. Thermal-orbital evolution of Io and Europa. Icarus 171 (2), 391–410. http://dx.doi.org/10.1016/j.icarus.2004.05.020.

Hussmann, H., Spohn, T., Wieczerkowski, K., 2002. Thermal equilibrium states of Europa's ice shell: Implications for internal ocean thickness and surface heat flow. Icarus 156 (1), 143–151. http://dx.doi.org/10.1006/icar.2001.6776, URL http://www.sciencedirect.com/science/article/pii/S0019103501967764.

Jackson, I., Faul, U.H., 2010. Grainsize-sensitive viscoelastic relaxation in olivine: Towards a robust laboratory-based model for seismological application. Phys. Earth Planet. Inter. 183 (1–2), 151–163. http://dx.doi.org/10.1016/j.pepi.2010.09.005, URL http://linkinghub.elsevier.com/retrieve/pii/S0031920110001871.

Jackson, I., Faul, U.H., Fitz Gerald, J.D., Tan, B.H., 2004. Shear wave attenuation and dispersion in melt-bearing olivine polycrystals: 1. Specimen fabrication and mechanical testing. J. Geophys. Res. B: Solid Earth 109 (6), 1–17. http://dx.doi.org/10.1029/2003JB002406.

Jackson, I., Faul, U.H., Skelton, R., 2014. Elastically accommodated grain-boundary sliding: New insights from experiment and modeling. Phys. Earth Planet. Inter. 228, 203–210. http://dx.doi.org/10.1016/j.pepi.2013.11.014, URL https://www.sciencedirect.com/science/article/pii/S0031920113001738.

Jackson, I., Fitz Gerald, J.D., Faul, U.H., Tan, B.H., 2002. Grain-size-sensitive seismic wave attenuation in polycrystalline Olivine. J. Geophys. Res.: Solid Earth 107 (B12), ECV 5–1–ECV 5–16. http://dx.doi.org/10.1029/2001JB001225, 2360.

Kamata, S., 2023. Poroviscoelastic gravitational dynamics. J. Geophys. Res: Planets 128 (7), http://dx.doi.org/10.1029/2022JE007700, e2022JE007700. URL https://onlinelibrary-wiley-com.ezproxy1.lib.asu.edu/doi/abs/10.1029/2022JE007700.

Karato, S.-I., 1984. Grain-size distribution and rheology of the upper mantle. Tectonophysics 104 (1), 155–176. http://dx.doi.org/10.1016/0040-1951(84)90108-2, URL https://www.sciencedirect.com/science/article/pii/0040195184901082.

Khan, A., Liebske, C., Rozel, A., Rivoldini, A., Nimmo, F., Connolly, J.a.D., Plesa, A.-C., Giardini, D., 2018. A geophysical perspective on the bulk composition of mars. J. Geophys. Res: Planets 123 (2), 575–611. http://dx.doi.org/10.1002/2017JE005371, URL https://onlinelibrary.wiley.com/doi/abs/10.1002/2017JE005371.

Knopoff, L., MacDonald, G.J.F., 1958. Attenuation of small amplitude stress waves in solids. Rev. Modern Phys. 30, 1178–1192. http://dx.doi.org/10.1103/RevModPhys.30.1178, URL https://link.aps.org/doi/10.1103/RevModPhys.30.1178.

Lainey, V., Arlot, J.-E., Karatekin, O., Van Hoolst, T., 2009. Strong tidal dissipation in Io and Jupiter from astrometric observations. Nature 459 (7249), 957–959. http://dx.doi.org/10.1038/nature08108.

Lau, H.C.P., Faul, U.H., 2019. Anelasticity from seismic to tidal timescales: Theory and observations. Earth Planet. Sci. Lett. 508, 18–29. http://dx.doi.org/10.1016/j.epsl.2018.12.009, URL https://www.sciencedirect.com/science/article/pii/S0012821X18307180.

Lau, H.C.P., Holtzman, B.K., 2019. "Measures of dissipation in viscoelastic media" extended: Toward continuous characterization across very broad geophysical time scales. Geophys. Res. Lett. 46 (16), 9544–9553. http://dx.doi.org/10.1029/2019GL083529, URL https://onlinelibrary.wiley.com/doi/abs/10.1029/2019GL083529.

McCarthy, C., Cooper, R.F., 2016. Tidal dissipation in creeping ice and the thermal evolution of Europa. Earth Planet. Sci. Lett. 443, 185–194. http://dx.doi.org/10.1016/j.epsl.2016.03.006, URL https://www.sciencedirect.com/science/article/pii/S0012821X16300930.

McCarthy, C., Takei, Y., 2011. Anelasticity and viscosity of partially molten rock analogue: Toward seismic detection of small quantities of melt. Geophys. Res. Lett. 38 (18), http://dx.doi.org/10.1029/2011GL048776, URL https://onlinelibrary.wiley.com/doi/abs/10.1029/2011GL048776.

McCarthy, C., Takei, Y., Hiraga, T., 2011. Experimental study of attenuation and dispersion over a broad frequency range: 2. the universal scaling of polycrystalline materials. J. Geophys. Res.: Solid Earth 116 (B9), http://dx.doi.org/10.1029/2011JB008384, URL https://agupubs.onlinelibrary.wiley.com/doi/abs/10.1029/2011JB008384.

Mitri, G., 2023. Ice dynamic recrystallization within Europa's ice shell: Implications for solid-state convection. Icarus 115648. http://dx.doi.org/10.1016/j.icarus.2023.115648, URL https://www.sciencedirect.com/science/article/pii/S0019103523002257.

Moore, W.B., 2006. Thermal equilibrium in Europa's ice shell. Icarus 180 (1), 141–146. http://dx.doi.org/10.1016/j.icarus.2005.09.005, URL http://www.sciencedirect.com/science/article/pii/S0019103505003544.

Moore, W.B., Schubert, G., 2000. The tidal response of Europa. Icarus 147 (1), 317–319. http://dx.doi.org/10.1006/icar.2000.6460, URL http://www.sciencedirect.com/science/article/pii/S0019103500964601.

Moore, W.B., Schubert, G., Anderson, J.D., Spencer, J.R., 2007. The interior of Io. In: Io After Galileo: A New View of Jupiter's Volcanic Moon. Springer Berlin Heidelberg, pp. 89–108. http://dx.doi.org/10.1007/978-3-540-48841-5_5.

Morris, S.J.S., Jackson, I., 2009. Diffusionally assisted grain-boundary sliding and viscoelasticity of polycrystals. J. Mech. Phys. Solids 57 (4), 744–761. http://dx.doi.org/10.1016/j.jmps.2008.12.006, URL https://www.sciencedirect.com/science/article/pii/S0022509608000223.

Murray, C.D., Dermott, S.F., 1999. Solar System Dynamics. Cambridge University Press.

Nimmo, F., 2004. Stresses generated in cooling viscoelastic ice shells: Application to Europa. J. Geophys. Res: Planets 109 (E12), http://dx.doi.org/10.1029/2004JE002347, arXiv:https://agupubs.onlinelibrary.wiley.com/doi/pdf/10.1029/2004JE002347.

Nimmo, F., Brown, M.E., 2023. The internal structure of eris inferred from its spin and orbit evolution. Sci. Adv. 9 (46), eadi9201. arXiv:https://www.science.org/doi/pdf/10.1126/sciadv.adi9201.

Nimmo, F., Faul, U., 2013. Dissipation at tidal and seismic frequencies in a melt-free, anhydrous Mars. J. Geophys. Res: Planets 118 (12), 2558–2569.

O'Connell, R.J., Budiansky, B., 1978. Measures of dissipation in viscoelastic media. Geophys. Res. Lett. 5 (1), 5–8. http://dx.doi.org/10.1029/GL005i001p00005, URL https://onlinelibrary-wiley-com.ezproxy1.lib.asu.edu/doi/abs/10.1029/GL005i001p00005.

Ojakangas, G., Stevenson, D., 1986. Episodic volcanism of tidally heated satellites with application to Io. Icarus 66 (2), 341–358. http://dx.doi.org/10.1016/0019-1035(86)90163-6, URL http://www.sciencedirect.com/science/article/pii/0019103586901636.

Peltier, W.R., 1996. Mantle viscosity and ice-age ice sheet topography. Science 273 (5280), 1359–1364. http://dx.doi.org/10.1126/science.273.5280.1359, URL https://www.science.org/doi/abs/10.1126/science.273.5280.1359.

Qu, T., Jackson, I., Faul, U.H., 2021. Low-frequency seismic properties of Olivine-orthopyroxene mixtures. J. Geophys. Res.: Solid Earth 126 (10), http://dx.doi.org/10.1029/2021JB022504, e2021JB022504. URL https://onlinelibrary.wiley.com/doi/abs/10.1029/2021JB022504.

Raj, R., Ashby, M., 1971. On grain boundary sliding and diffusional creep. Metall. Trans. 2, 1113–1127.

Ray, R.D., Eanes, R.J., Lemoine, F.G., 2001. Constraints on energy dissipation in the earth's body tide from satellite tracking and altimetry. Geophys. J. Int. 144 (2), 471–480. http://dx.doi.org/10.1046/j.1365-246x.2001.00356.x, arXiv:http://gji.oxfordjournals.org/content/144/2/471.full.pdf+html.

Renaud, J.P., 2019. A Study of the Tidal and Thermal Evolution of Rocky & Icy Worlds Utilizing Advanced Rheological Models (Ph.D. thesis). George Mason University, p. 164.

Renaud, J.P., Henning, W.G., 2018. Increased tidal dissipation using advanced rheological models: Implications for io and tidally active exoplanets. Astrophys. J. 857 (2), 98. http://dx.doi.org/10.3847/1538-4357/aab784.

Rhoden, A.R., Walker, M.E., 2022. The case for an ocean-bearing Mimas from tidal heating analysis. Icarus 376, 114872. http://dx.doi.org/10.1016/j.icarus.2021.114872, URL https://www.sciencedirect.com/science/article/pii/S0019103521005091.

Roberts, J.H., Nimmo, F., 2008. Tidal heating and the long-term stability of a subsurface ocean on enceladus. Icarus 194 (2), 675–689. http://dx.doi.org/10.1016/j.icarus.2007.11.010.

Sabadini, R., Peltier, W.R., 1981. Pleistocene deglaciation and the earth's rotation: Implications for mantle viscosity. Geophys. J. Int. 66 (3), 553–578. http://dx.doi.org/10.1111/j.1365-246X.1981.tb04890.x.

Sailor, R.V., Dziewonski, A.M., 1978. Measurements and interpretation of normal mode attenuation. Geophys. J. R. Astron. Soc. 53 (3), 559–581. http://dx.doi.org/10.1111/j.1365-246X.1978.tb03760.x, URL https://onlinelibrary.wiley.com/doi/abs/10.1111/j.1365-246X.1978.tb03760.x.

Saxena, P., Renaud, J.P., Henning, W.G., Jutzi, M., Hurford, T., 2018. Relevance of tidal heating on large TNOs. Icarus 302, 245–260. http://dx.doi.org/10.1016/j.icarus.2017.11.023, URL http://www.sciencedirect.com/science/article/pii/S0019103517303858.

Shoji, D., Hussmann, H., Kurita, K., Sohl, F., 2013. Ice rheology and tidal heating of Enceladus. Icarus 226 (1), 10–19. http://dx.doi.org/10.1016/j.icarus.2013.05.004, URL https://www.sciencedirect.com/science/article/pii/S0019103513002042.

Sotin, C., Head III, J.W., Tobie, G., 2002. Europa: Tidal heating of upwelling thermal plumes and the origin of lenticulae and chaos melting. Geophys. Res. Lett. 29 (8), 74–1–74–4. http://dx.doi.org/10.1029/2001GL013844, URL https://onlinelibrary.wiley.com/doi/abs/10.1029/2001GL013844.

Sotin, C., Tobie, G., Wahr, J., McKinnon, W.B., 2009. Tides and tidal heating on Europa. In: Pappalardo, R.T., McKinnon, W.B., Khurana, K. (Eds.), In: Europa, vol. 11, University of Arizona press Tucson, pp. 85–117.

Sundberg, M., Cooper, R.F., 2010. A composite viscoelastic model for incorporating grain boundary sliding and transient diffusion creep; Correlating creep and attenuation responses for materials with a fine grain size. Phil. Mag. 90 (20), 2817–2840. http://dx.doi.org/10.1080/14786431003746656.

Takei, Y., Karasawa, F., Yamauchi, H., 2014. Temperature, grain size, and chemical controls on polycrystal anelasticity over a broad frequency range extending into the seismic range. J. Geophys. Res.: Solid Earth 119 (7), 5414–5443. http://dx.doi.org/10.1002/2014JB011146, URL https://onlinelibrary.wiley.com/doi/abs/10.1002/2014JB011146.

Tan, B.H., Jackson, I., Fitz Gerald, J.D., 2001. High-temperature viscoelasticity of fine-grained polycrystalline Olivine. Phys. Chem. Miner. 28 (9), 641–664. http://dx.doi.org/10.1007/s002690100189.

Tobie, G., Mocquet, A., Sotin, C., 2005. Tidal dissipation within large icy satellites: Applications to Europa and Titan. Icarus 177 (2), 534–549. http://dx.doi.org/10.1016/j.icarus.2005.04.006, Europa Icy Shell. URL http://www.sciencedirect.com/science/article/pii/S0019103505001582.

Walterová, M., Běhounková, M., Efroimsky, M., 2023a. Is there a semi-molten layer at the base of the lunar mantle? J. Geophys. Res: Planets n/a (n/a), http://dx.doi.org/10.1029/2022JE007652, e2022JE007652. URL https://onlinelibrary.wiley.com/doi/abs/10.1029/2022JE007652.

Walterová, M., Plesa, A.-C., Wagner, F.W., Breuer, D., 2023b. Andrade rheology in planetary science. Authorea Preprints, Authorea.

Weber, R.C., Lin, P.-Y., Garnero, E.J., Williams, Q., Lognonné, P., 2011. Seismic detection of the Lunar core. Science 331 (6015), 309–312. http://dx.doi.org/10.1126/science.1199375, arXiv:http://science.sciencemag.org/content/331/6015/309.full.pdf.

Williams, J.G., Boggs, D.H., 2015. Tides on the moon: Theory and determination of dissipation. J. Geophys. Res: Planets 120 (4), 689–724. http://dx.doi.org/10.1002/2014JE004755, URL https://onlinelibrary.wiley.com/doi/abs/10.1002/2014JE004755.

Williams, J.G., Konopliv, A.S., Boggs, D.H., Park, R.S., Yuan, D.-N., Lemoine, F.G., Goossens, S., Mazarico, E., Nimmo, F., Weber, R.C., Asmar, S.W., Melosh, H.J., Neumann, G.A., Phillips, R.J., Smith, D.E., Solomon, S.C., Watkins, M.M., Wieczorek, M.A., Andrews-Hanna, J.C., Head, J.W., Kiefer, W.S., Matsuyama, I., McGovern, P.J., Taylor, G.J., Zuber, M.T., 2014. Lunar interior properties from the GRAIL mission. J. Geophys. Res: Planets 119 (7), 1546–1578. http://dx.doi.org/10.1002/2013JE004559, 2013JE004559.

Xiao, C., Wu, Y., Yan, J., Harada, Y., Zhang, Y., Li, F., 2022. Comparison of the effects of different viscoelastic and temperature models on the theoretical tidal response of the moon. J. Geophys. Res: Planets 127 (12), http://dx.doi.org/10.1029/2022JE007215, e2022JE007215. URL https://onlinelibrary.wiley.com/doi/abs/10.1029/2022JE007215.

Yamauchi, H., Takei, Y., 2016. Polycrystal anelasticity at near-solidus temperatures. J. Geophys. Res.: Solid Earth 121 (11), 7790–7820. http://dx.doi.org/10.1002/2016JB013316, URL https://onlinelibrary.wiley.com/doi/abs/10.1002/2016JB013316.

Yoder, C.F., 1979. How tidal heating in Io drives the Galilean orbital resonance locks. Nature 279 (5716), 767–770. http://dx.doi.org/10.1038/279767a0, URL https://www.nature.com/articles/279767a0.

Yoder, C.F., Konopliv, A.S., Yuan, D.N., Standish, E.M., Folkner, W.M., 2003. Fluid core size of mars from detection of the solar tide. Science 300 (5617), 299–303. http://dx.doi.org/10.1126/science.1079645, arXiv:https://www.science.org/doi/pdf/10.1126/science.1079645.